Influence of the fiber drawing process on mechanical and vibrational properties of sol-gel silica glass

Francesca Cova[a,*], Alessandro Benedetto[b], Norberto Chiodini[a], Roberto Lorenzi[a], Anna Vedda[a], Vladimir Ouspenski[b]

[a] *Department of Materials Science, University of Milano - Bicocca, Via Cozzi 55, 20125 Milan, Italy*
[b] *Saint-Gobain Research Paris, 39 quai Lucien Lefranc, 93303 Aubervilliers Cedex, France*

Abstract

The influence of fiber drawing on mechanical and vibrational properties of RE-doped sol-gel silica is disclosed by a comparison of bulk silica, before and after the melting process, and fibers.

The mechanical characterization is carried out by nanoindentation technique: hardness and elastic modulus are found to be consistent with those of Corning7980 reference glass, and related to the elasto-plastic behavior of the glassy material. Our results evidence an increase of the resistance of fibers to fracture under an applied load, ascribed to drawing-induced residual stresses. Their impact on sol-gel silica mechanical properties is further disclosed by complementary vibrational characterization by Raman and FTIR spectroscopies, confirming the occurrence of a modification of the structural features after the drawing process and of residual stresses in the fibers.

The overall results highlight the role of the fiber drawing in improving the glass mechanical properties, causing a slight rearrangement of the silica structure.

Keywords: optical fibers, sol-gel, silica glass, nanoindentation, Raman spectroscopy, FTIR spectroscopy

2010 MSC: 82D30, 78A45, 74C05

1. Introduction

Recent studies demonstrated that the sol-gel synthesis technique allows to achieve a good rare earth (RE) ions incorporation and dispersion inside the glass matrix for RE concentrations below 1 mol% [1]; only for higher concentrations, the formation of RE-rich nanocrystalline clusters, affecting the glass homogeneity, was observed [2, 3, 4]. Moreover, the glass synthesis by sol-gel method can be performed by using high purity precursors, thus reducing the level of unwanted impurities and aiming at a good control of the material defectiveness. Therefore, RE-doped silica glasses prepared by sol-gel route were recently shown to be suitable materials for the realization of scintillating optical fibers, opening their application perspectives for real-time dosimetry in the medical field [5, 6], as well as for

*Corresponding author
Email address: francesca.cova@unimib.it (Francesca Cova)

high-energy physics experiments [7], with a special focus on the simultaneous dual-readout approach for the improvement of the calorimeters energy resolution [8]. Praseodymium and Cerium ions have been considered as promising luminescent activators because of their fast allowed transition from the $5d$ excited level to the $4f$ ground state, leading to emission bands in the UV-blue spectral region.

During fiber drawing [9], the silica glass preform is heated close to its melting temperature under an applied axial tension; upon exiting the furnace, the temperature of the fiber is abruptly lowered down from around its melting point of 1980 K to below 500 K. This drastic temperature drop in the glass has been demonstrated to bring about residual stresses in the drawn silica fibers, persisting even when no external forces are applied and originating partially from the difference in the thermal and mechanical properties between the core and the cladding [10, 11, 12, 13]. On the other hand, the harsh temperature conditions experienced during the drawing process have been proven to maintain the amorphous character of silica network and a good dispersion of RE dopant ions [14]. However, a careful comparison of the fiber and bulk glass properties could reveal differences especially in the mechanical and vibrational features; in fact, a readjustment of the SiO_2 network, induced by the high temperature treatment associated with the drawing procedure, is expected to occur. The process could indeed affect, either negatively or positively, the defectiveness of the glass network, with several consequences in the material characteristics, such as the mechanical performances and the local environment surrounding the luminescent centers.

The effect of the fiber drawing on the resistance to ionizing radiation damage has been extensively discussed for pure silica-core fibers [15, 16, 17], polymer-clad silica fibers [18], and sol-gel silica [7, 19]: especially in the latter case, the drawing process turned out to positively induce a reduction of the concentration of radiation-induced defect precursors, leading to an improvement of the resistance to radiation damage for what concerns the scintillation performances. This result is a promising essential feature for scintillation applications that involve high levels of irradiation dose.

The investigation of the mechanical properties of sol-gel silica can be included in the framework of the so-called anomalous behavior of glasses, of which fused silica is the most significant example [20, 21]: the accepted explanation for the anomalous behavior of silica lies in the tetrahedral bond structure of the basic silica network, which allows relative motions of the atoms of the Si-O-Si linkages. The distinction between normal and anomalous behavior extends from the mechanical and thermal properties to the material deformation and fracture characteristics: these properties have been demonstrated to be highly dependent on the spatial arrangement of the silica tetrahedra [22]. Anomalous glasses are expected to show densification under an applied external load and reduced residual stresses at the indentation site, with consequently shortened radial cracks length, compared to normal glassy materials.

In this work, we present the mechanical properties of sol-gel silica fibers compared to those of the parent bulk glass, in order to disclose the role of the fiber drawing on the characteristics and performances of this material. A detailed characterization has therefore been carried out by the nanoindentation technique on different glass samples, from preforms to fibers through intermediate drawing stages, since few studies have been reported so far on sol-gel silica, especially in the fiber form. The comparison with reference glass is then exploited to discuss the obtained

results. These studies are complemented by Raman and Fourier Transform Infrared (FTIR) analyses, in order to investigate the influence of the drawing process on the vibrational features of sol-gel silica and to confirm the presence of residual stresses derived from the thermal history experienced by sol-gel silica during the fiber drawing: a qualitative correlation with the nanoindentation outcome is then established.

2. Materials and Methods

Pr-doped silica glass with concentration of 0.05 mol% and Ce-doped silica glasses with Ce concentrations of 0.0125 mol% or 0.05 mol% were prepared by sol-gel method using tetramethylortosilicate (TMOS) and Pr,Ce(III) as precursors. Alcogels were obtained after gelation and subsequently dried in a thermostatic chamber for a few weeks. The obtained xerogels were densified up to 1225 °C, in order to obtain doped preforms with dimensions of 70 mm in length and 10 mm in diameter.

Pr-doped and 0.05 mol% Ce-doped preforms were then drawn into fibers by Polymicro Technologies (Phoenix, USA), while the 0.0125 mol% Ce-doped preform was drawn by the Optoelectronic Research Center (Southampton, UK): a fluorinated SiO_2 cladding wrapping the RE-doped core was used in order to guarantee a good light guiding by the core-cladding interface.

Seven samples were considered and compared in this work, varying in their characteristics and experienced treatments. The first one was obtained as a 0.5 mm slice of the 70 mm long Pr-doped bulk preform prior to the drawing. Two other samples with thickness of 1.8 mm and 2.5 mm were cut from the leftover of the fiber drawing process of the 0.05 mol% Ce-doped silica preform: only the 1.8 mm thick one was irradiated with X-rays up to 1 kGy. Another sample with thickness of 2.3 mm was cut from the leftover of the fiber drawing process of the 0.05 mol% Pr-doped silica preform. Eventually, three 10 mm long pieces of silica fibers fully drawn to the desired diameter, doped with 0.05 mol% Pr, 0.05 mol% Ce, and 0.0125 mol% Ce, were embedded in epoxy resin and measured. Similar outcomes were obtained at varying dopant specie and Ce concentration: therefore, only the results concerning the 0.05 mol% Ce-doped fiber were reported in the following. A Corning 7980 synthetic glass commonly used as reference for the nanoindentation analysis was also measured, in order to better characterize the properties of silica glass obtained by a more recently developed sol-gel synthesis method, of which only few studies discussed the mechanical behavior.

Fig. 1 schematically shows a sketch of the neck-down from the preform dimension to the final fiber diameter: the approximate positions of the samples along the fiber neck-down are also displayed. The intermediate samples are denoted hereafter as melted samples: they have a similar thermal history with respect to the fibers, because they both experienced the high temperature treatment of the drawing process. While the fiber pieces are cut from the fiber completely drawn to the final diameter, the melted samples are taken from the leftover remaining in the drawing neck-down. Therefore, they can be considered as residuals of the drawing, and their properties intermediate with respect to the pristine preform and the fully drawn fiber.

Nanoindentation measurements were performed using Hysitron Ti960 nanoindenter. Two different measurement

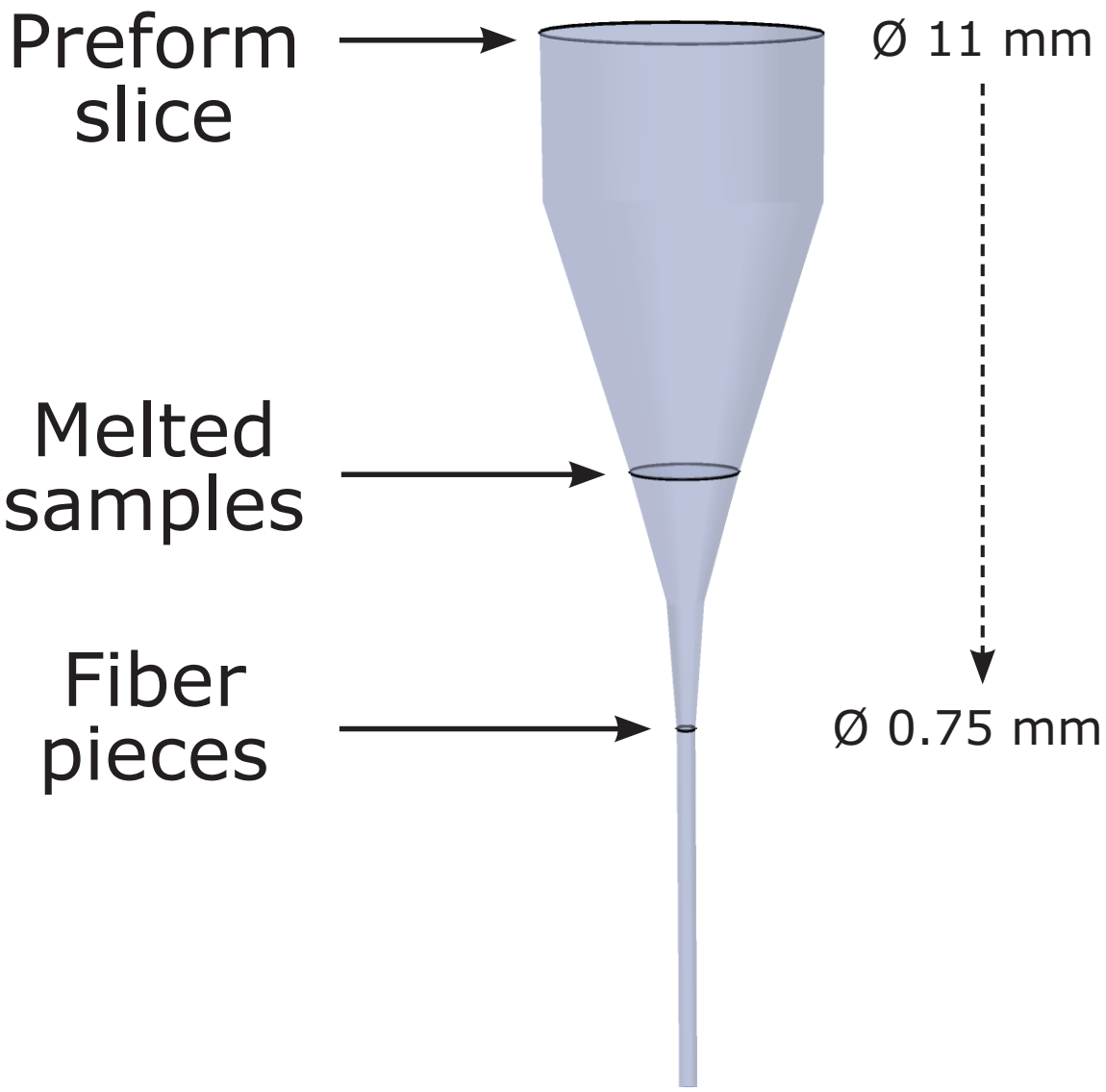

Figure 1: Schematic sketch of the final part of a drawn preform. The investigated samples were taken as representatives of different stages of the drawing process. The initial and final diameter are reported in the figure.

heads were used depending on the maximum applied load. The standard instrument head was used for loads up to 10 mN: this head combines a piezoelectric scanner for "coarse" head displacement and a capacitive transducer for tip loading and fine displacement. An Omniprobe that allows for indents up to 500 mN was used for higher loads. Omniprobe uses an inductive system in order to control force and to measure tip displacement. For hardness and elastic modulus measurements we used diamond Berkovich tips (triangular pyramid with total included angle 142.3°). Diamond corner-cube tips (triangular pyramid with total included angle 90°) were used for toughness measurement from crack lengths. Tips were provided by Synton-MDP (Switzerland). The area function was calibrated by indentation on Corning 7980 synthetic glass by using the standard procedure described in [23]. Indents were performed using a standard "trapezoidal" load function with a loading rate of 200 μN/s, a hold time of 2 s and an unloading rate of 200 μN/s. All the samples were measured in cross-section: one side of the sample slice was glued with a proper glue for nanoindentation testing to the instrument table, made of stainless steel, which is placed and fixed under the tip; the other side directly faced the indenter tip. The latter was previously optically polished to avoid high levels of roughness. The same procedure applied for fibers embedded in epoxy resin: in this case, the measurement in cross-section allowed to separately evaluate the different properties of the core and the cladding. Data analysis, to extract elastic modulus and hardness, was also done with the well-established model proposed by [23]. Images for crack length measurements were performed recording topography after indentation by sweeping the tip thanks to the piezoelectric scanner in the standard indentation head: 2 μN was set as scanning load. "Gradient" images were also recorded by measuring deviations in normal force during feedback loop control as they allow for easier detection of edges and cracks. The length of the cracks was then evaluated by the analysis of the raster scan images of the residual impressions by ImageJ software [24].

Raman spectra were recorded at room temperature (RT) by a micro-Raman spectrometer (Labram, Jobin-Yvon), equipped with a microscope; the excitation source was an internal He-Ne laser at 632.8 nm, and the unpolarized Raman spectra were collected in back-scattering configuration through a CCD (charge coupled device) detector and corrected for spectral response of the apparatus.

FTIR spectra were recorded with a micro-FTIR Nicolet iN10, using two geometries: in the range 2000 - 4000 cm^{-1} the spectra were collected in transmission mode, while the range 400 - 2000 cm^{-1} was investigated in reflection mode. The spectral resolution was 4 cm^{-1} and at least 128 accumulations were used. The sampled area was 300 μm x 300 μm.

3. Results and Discussion

3.1. Mechanical properties by nanoindentation technique

The nanoindentation technique is a powerful tool for determining the mechanical properties of materials at nanometric scale, like the hardness, the elastic modulus, and the toughness. The mechanical parameters can be evaluated directly from the measurement of the indentation load and of the indenter tip displacement on the material surface;

this feature makes the technique largely attractive, allowing an insight of the elastic-plastic behavior of materials, and a measurement of the residual stress levels. Exhaustive reviews of the nanoindentation method, from its introduction to the latest advancements, can be found in [23, 25].

Images of the residual impressions left on the material surface after a nanoindentation measurement are reported in Fig. 2. The images were used to evaluate the length of the cracks developing from the indentation corners, when occurring. In panels (a) and (b), the maximum load of 9 mN was chosen as example for the images to be shown, but residual impression images were recorded for all the measurements carried out at varying load, in the 1 - 10 mN range with 1 mN step. The distance between each indentation is 20 μm. For the bulk preform (panel a), the nanoindentation test did not provide any useful result, because of the blurry residual impression image, probably due to the poor quality of the sample surface, which turned out to be isotropically rough even after polishing. This observation can be ascribed to the absence of any high temperature treatment on this sample. The formation of cracks is visible for the melted sample (panel b): a threshold load at which the first cracks appear does not exist for the melted sample, since cracks formed even at the minimum considered loads. On the other hand, in the case of the fiber (panels c and d), the cracks started to develop when a threshold applied load is reached, as described in the following. This phenomenon suggests that the drawing process induces an increase of the mechanical resistance of silica to applied external loads.

A second set of measurements was therefore performed on fibers by increasing the maximum applied load in the range 10 - 100 mN, with 5 mN step; this test revealed that the threshold load for fibers was around 20 mN. An example of residual impression image from this second set of nanoindentations is shown in panel (c) for a maximum applied load of 35 mN. The presence of a threshold load for cracks formation points towards the existence of compressive residual stresses and to the increase of the toughness in the fibers, with respect to the other silica samples [26]. Above 60 mN, the nanoindentation impression images did not provide any useful information for the evaluation of the cracks length, because of the occurrence of a high level of chipping, as displayed in panel (d).

Cracks formed under a cube-corner indentation are “quadrant” or quarter-penny shaped: it was demonstrated that the length of cube-corner indentation cracks can provide a good estimate of residual stresses sampled over small volumes [27]. It is the residual component of the contact stress field that determines indeed the ultimate radial crack size. In Fig. 3(a), the characteristic dimensions of quarter penny-like radial/median cracks are sketched. Moreover, from the direct measurement of the crack traces c on the indented surface as a function of the load P, the toughness K_c can be calculated via Eq. 1, where E is the Young modulus and H the hardness; Eq. 1 is valid only in the case of a cube-corner indenter tip geometry [28].

$$K_c = 0.036\sqrt{\frac{E}{H}}\frac{P}{c^{3/2}} \tag{1}$$

The toughness is an important fracture parameter, defined as the ability of a material to absorb energy and plastically deform without fracturing.

In Fig. 3(b), the average cube-corner indentation crack length as a function of load is reported, comparing Ce- and Pr-doped sol-gel silica (full symbols), and Ce-doped silica before and after 1 kGy X-ray irradiation (black round

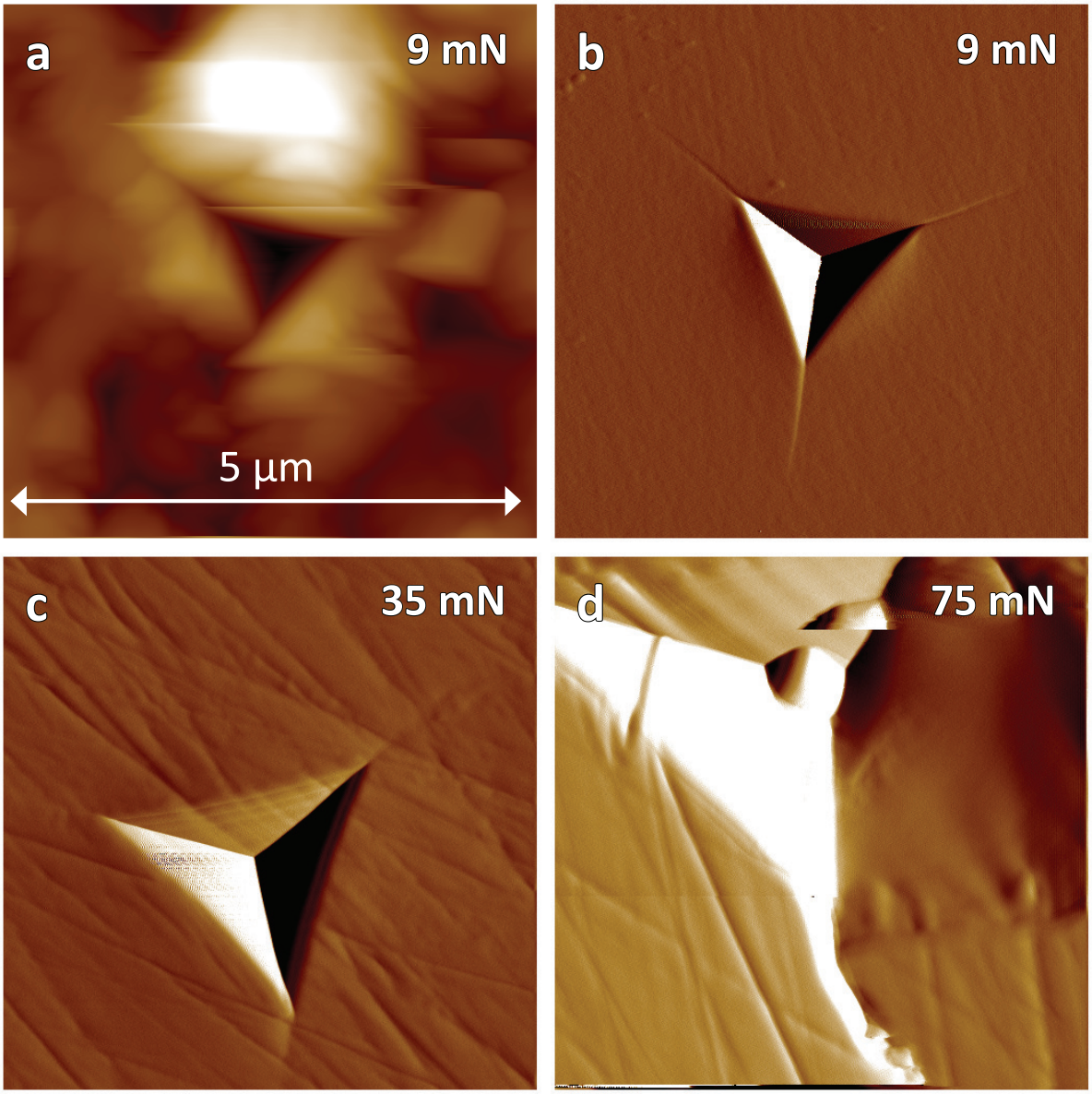

Figure 2: Raster scan of the residual impressions after an indentation measurement in sol-gel silica glass, performed recording topography by sweeping the tip thanks to the piezoelectric scanner in the standard indentation head: 2 μN was set as scanning load. The indenter was a cube-corner tip and the width of field was 5 μm. (a) Pr-doped sol-gel silica preform, applied load 9 mN. (b) Ce-doped sol-gel silica melted sample, applied load 9 mN. (c) Ce-doped sol-gel silica fiber core, applied load 35 mN. (d) Ce-doped sol-gel silica fiber core, applied load 75 mN: in this case, the presence of chipping prevented the accurate measurement of crack length.

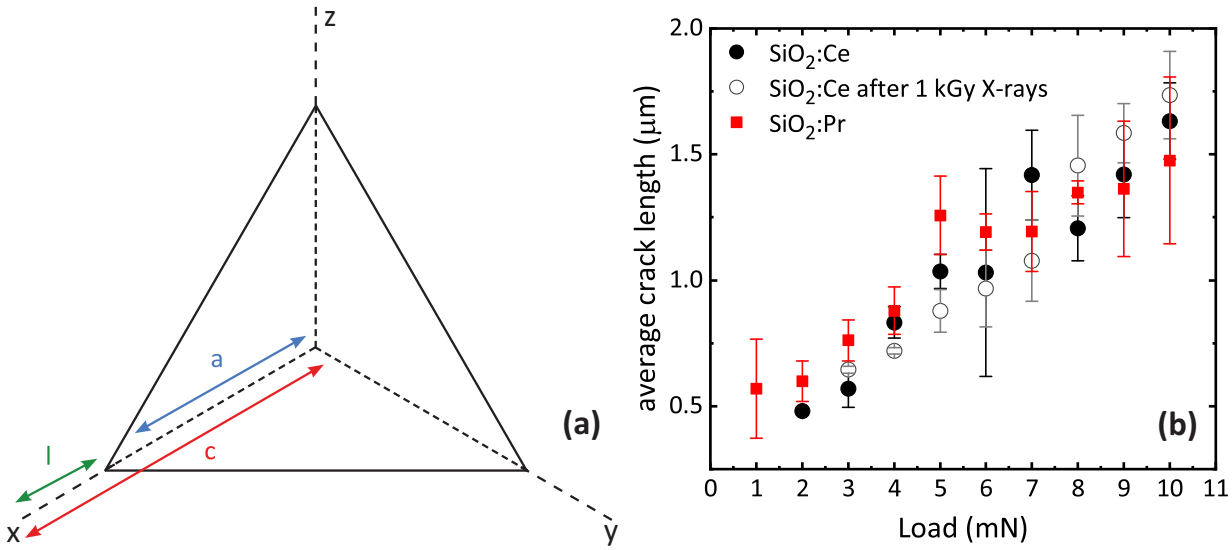

Figure 3: Left panel: schematic of a cube-corner indentation site. The dashed lines represent the cracks occurring at each corner site when the threshold load for the investigated material is reached. The hardness impression with the characteristic dimensions l, a, and c of quarter-penny like radial/median crack is shown. Right panel: crack length as a function of increasing maximum applied load. Each data point corresponds to the average over the three cracks developing from the indentation corners; the crack traces corresponding to the parameter c of the left panel have been considered. Melted samples doped with two different RE ions, namely Ce and Pr are compared; for the same Ce-doped silica melted sample, the effect of X-ray irradiation is also investigated.

symbols). The incorporation of Pr ions, with respect to Ce ions, does not seem to influence the nanoindentation response; moreover, the X-ray irradiation does not turn out to affect the mechanical behavior of sol-gel silica, since the obtained values are similar, taking into account the measurements uncertainties. The choice of the dose value to test was made in accordance with our previous results [7, 19], which evidenced a relevant radiation damage on the optical properties of sol-gel silica at a dose of the order of 1 kGy, that is significant for the application of silica glasses as scintillators.

The so-called load-displacement curves are shown in Fig. 4, displaying the depth reached by the tip in the surface deformation as the applied load increases up to the maximum set value (loading segment); during the unloading process, the applied load is gradually released and the deformation is partially recovered, so that the depth of the indenter decreases. In Fig. 4, the load-displacement curves are reported as a function of increasing maximum applied load in the 1 - 10 mN range (left panel) for the non-irradiated Ce-doped silica melted sample, and as a function of the stage of the drawing process the samples come from (right panel), as reported in the legend. For the bulk sample, no significant results were obtained, as explained above: therefore, only the curves related to the melted and the fiber samples are displayed. Since the indenter tip is very sharp, it was possible to separately measure the fiber core and cladding, in order to check the influence of fluorine on the hardness of silica: the mechanical behavior of the fiber cladding can therefore be located in between that of the melted sample and that of the fiber core. Despite the

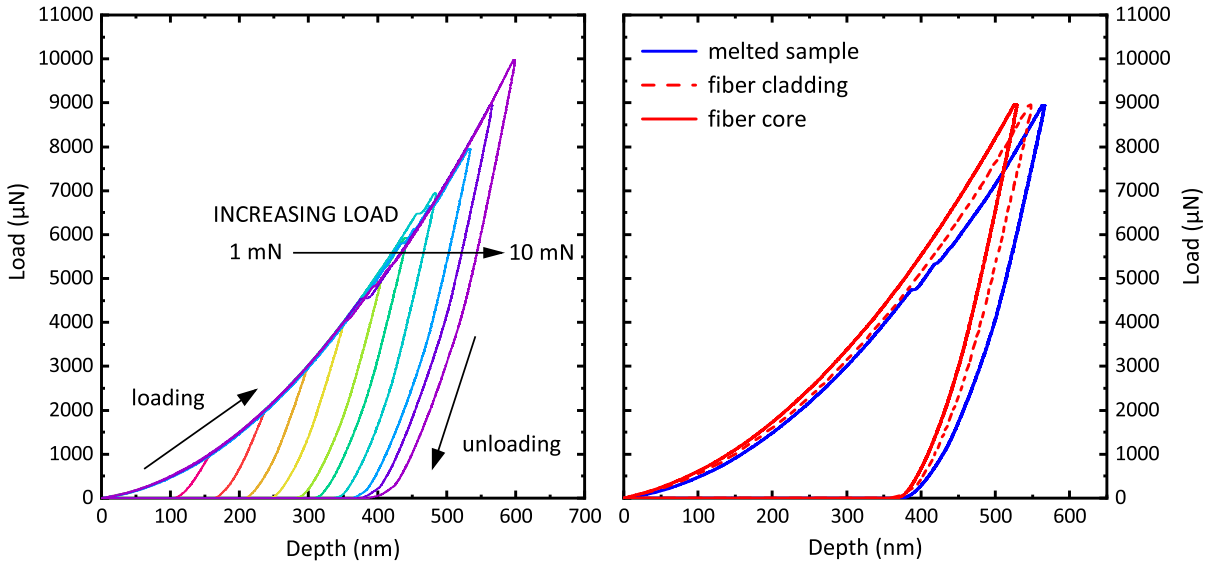

Figure 4: Load-displacement curves for nanoindentation measurements in sol-gel silica, showing elastic-plastic behavior. Left panel: load-displacement curves as a function of increasing maximum applied load for the non-irradiated Ce-doped silica melted sample. The formation of cracks leads to the presence of a step along the loading segment of the curves related to the highest applied loads. Right panel: load-displacement curves for samples from different stages of the drawing process, listed in the legend. The maximum applied load was 9 mN.

difference in composition and synthesis method between the fluorinated silica cladding and the sol-gel silica core of the fiber, the mechanical behavior of the cladding has to be taken into account because it is a significant component of the final fiber that can influence its overall application-oriented properties and performances. Indeed, a shift of the load-displacement profiles towards increasing hardness can be clearly pointed out when comparing the melted sample and the fiber curves: the application of the same maximum load of 9 mN led to a decrease of the maximum penetration depth achieved in the fiber cladding and even more in the fiber core.

Moreover, a step appears in the portion of the curve related to the loading phase, well observable for the highest applied loads in the left panel: it is due to the formation and development of cracks. In the ideal case of a fully elastic contact, the unloading curve should be superimposed to the loading segment. In the case of sol-gel silica, an elastic-plastic contact occurs: indeed, the unloading curve is well-distinguished from the loading one and the area enclosed between them represents the energy lost as heat during plastic deformation. During unloading there is some degree of elastic recovery as the elastically strained material outside of the plastic zone relaxes and tries to resume its original shape: in the load-displacement curves, this is evidenced by a reduction in displacement with decreasing load. Elastic recovery is prevented from happening entirely by the presence of the plastic zone; residual impressions thus remain in the surface, like those reported in Fig. 2. Therefore, deformation during unloading is demonstrated to be both elastic and plastic in nature.

Assuming a sharp transition from elastic to plastic behavior, the load-displacement curve can be modeled accord-

ing to [25]:

$$P = E^* \left[\frac{1}{\sqrt{\pi}\tan\alpha} \sqrt{\frac{E^*}{H}} + \left(\frac{2(\pi-2)}{\pi} \right) \sqrt{\frac{\pi}{4}} \sqrt{\frac{H}{E^*}} \right]^{-2} h^2 \tag{2}$$

where P is the load, E^* is the effective elastic modulus, H is the hardness, assumed to be constant, α is the equivalent cone angle dependent on the indenter tip, and h is the displacement. The hardness is the resistance to localized plastic deformation induced by either mechanical indentation or abrasion: it is dependent on the material microdurability and cannot be considered a fundamental material property. The elastic modulus E^* measures the resistance of a material to be elastically deformed when a stress is applied and is evaluated as the combined elastic modulus of the contacting bodies, namely the indenter and the sample: the indenter is usually made of diamond, thus being E^* dominated by the elastic properties of the investigated specimen for most materials. It can be calculated *via* Eq. 3: this formulation takes into account the occurrence of elastic displacements in both materials.

$$\frac{1}{E^*} = \frac{(1-\nu^2)}{E} + \frac{(1-\nu'^2)}{E'} \tag{3}$$

E' = 1141 GPa and ν' = 0.07 are the elastic modulus and Poisson's ratio of the diamond indenter, respectively. The value of ν = 0.17 for fused silica has been considered for the calculation of E^* [29].

In order to evaluate the hardness and the elastic modulus of sol-gel silica, the initial part of the unloading curve is the most significant: in principle, the two parameters can be obtained by fitting a polynomial expression of the second order to the unloading data, according to Eq. 2, and finding the derivative and the slope. However, it can be observed that the unloading response is fairly linear in the initial part, and thus the contact appears to have a linear dependence on the load, justifying the use of a linear fit to the upper portion of the unloading data, namely between 45 % and 90 % of the maximum.

In Table 1, the parameters describing the mechanical properties of silica samples are listed and compared to those related to a sample of bulk glass Corning 7980 used as reference. Nanoindentation measurements on the preform sample were affected by a poor quality of the rough surface; therefore, a higher uncertainty is associated to the obtained parameters, ascribed to a greater scattering of the data. We underline that the parameters obtained for sol-gel silica samples are close to those of the reference bulk glass and in good agreement with the values reported in the literature [30, 31]. Furthermore, a slight increase of the values of H and E was evidenced in the fiber, compared to the other samples, thus confirming a strengthening of the hardness induced by the fiber drawing process, which involves high temperature treatments coupled to fast cooling rates. The toughness could be evaluated only when the formation of cracks occurred: also in this case, the value of K_c resulted to be higher in the fiber.

In the following sections, the discussion of the modifications of sol-gel silica structural properties, induced by the fiber drawing process, is delved deeper through the investigation of the vibrational features by means of Raman and FTIR spectroscopies. The vibrational spectra help to deepen the understanding of the mechanical nanoindentation results reported so far and to correlate the existence of drawing-induced residual stresses with the observation of a

Table 1: Average values of hardness, elastic modulus, and toughness evaluated for sol-gel silica samples measured by nanoindentation. Missing data where no formation of cracks was observed. The high uncertainty associated to the toughness data can be ascribed to the great scattering of crack length values.

	Corning 7980	Preform	Melted	Fiber
H (GPa)	8.6 ± 0.5	8.2 ± 2.3	8.1 ± 0.4	9.3 ± 0.7
E (GPa)	72 ± 3	78 ± 11	73 ± 3	79 ± 3
K_c (Pa $\cdot$ m$^{0.5}$)	580 ± 130		547 ± 100	875 ± 260

mechanical strength increase in the fibers, compared to bulk silica.

3.2. Vibrational properties by Raman and FTIR spectroscopy

Raman spectra of RE-doped sol-gel silica at different stages of the drawing process are displayed in Fig. 5, normalized to the ω_3 band maximum: the labels refer to the vibrational assignments, made according to the literature [32, 33]. General features resembling those corresponding to pure silica glass can be detected: Raman structures of SiO_2 are observed at about 440, 800, and 1100 cm^{-1} (ω_1, ω_3, and ω_4 bands, respectively), corresponding to the Si - O rocking vibration of bridging oxygens, to the mixed stretching-bending Si - O vibration, and to transverse optical and longitudinal optical antisymmetric stretching, respectively [34, 35, 36]. The band at around 1100 cm^{-1} is more prominent in the FTIR spectra and is described in detail below. The D_1 and D_2 peaks at 490 and 610 cm^{-1} are due to the symmetric breathing modes of fourfold and threefold planar tetrahedra rings of SiO_2 [37]. No crystalline aggregates are evidenced, confirming that the fiber drawing process does not modify the amorphous character of the silica network and keeps a good dispersion of RE ions. The ω_1, also called R-band, is very sensitive to the Si-O-Si motion in larger rings (≥ 5) and gives insights about the overall bonding structure of the amorphous network. Passing from preform to melted and fiber samples, we observed a reduction of the ω_1 intensity accompanied by a slight shift to higher wavenumbers as expected from silica undergoing to thermal treatments [38], densification [39, 40], or fiber pulling [14, 41]. This evidence indicates a reduction of the main Si-O bond angle [40] which is more evident from preform to melted samples, while the fiber drawing introduces only minor differences in the ω_1 band structure. Moreover, the relative intensity of the ω_1 band with respect to the D_1 peak is higher in bulk with respect to the melted sample and to the fiber, in accordance with the results of a study of silica samples subjected to thermal treatments at different temperatures, where the formation of fourfold and threefold rings of SiO_2 tetrahedra was found to increase exponentially by temperature increasing [32]. A behavior similar to that reported in [14] of the D_1 peak intensity compared to that of the ω_1 band as a function of the stage of the drawing process can be observed in Fig. 5: indeed, in the fiber sample the intensities of the two structures are comparable, whereas the amplitude of the ω_1 band is more pronounced in the preform slice.

Moreover, in the samples subjected to high temperature treatments (melted and fiber samples), Raman D_1 and D_2 peak positions were found to slightly shift to higher wavenumbers without any decrease of the peak width with respect to

Table 2: Position of the maximum of the D_1 and D_2 Raman peaks for the three samples investigated. A slight shift to higher wavenumbers occurs in the thermally treated samples.

	Preform	Melted	Fiber
D_1 (cm^{-1})	486.6	487.7	488.7
D_2 (cm^{-1})	600.1	601.9	602.2

Table 3: Concentration of residual OH groups in the three sol-gel silica samples taken from different stages of the fiber drawing. The evaluation of the OH content was made following the procedure illustrated in [42].

	Preform	Melted	Fiber
OH content (ppm)	300	180	160

that of the bulk preform, as illustrated in Table 2 and further discussed in the next section.

As a further investigation of the vibrational properties of sol-gel silica, FTIR spectroscopy has been applied besides Raman measurements to detect the vibrational spectra of the OH groups, as belonging either to residual H_2O or to Si-OH, and the possible variation of the OH content as a consequence of the high temperature treatment experienced during fiber drawing. FTIR spectra in the 700 - 4000 cm^{-1} region are reported in Fig. 6, in reflection (left panel) and transmission (right panel) mode, for three RE-doped silica samples belonging to various stages of the drawing process, as reported in the legend, and already measured by Raman spectroscopy. The feature at around 800 cm^{-1} can be ascribed to the fundamental bending mode of Si-O-Si groups and related to the ω_3 band in the Raman spectra. The fundamental stretching mode (ν_1) at 1120 cm^{-1} is in good agreement with the weak ω_4 Raman band and here it is more clearly identified as related to the Si-O-Si bond antisymmetric stretching; the transverse (TO) and longitudinal (LO) optical modes are labeled in the Figure. Its overtone (ν_2) is visible at 2260 cm^{-1}, along with the Si-OH symmetric and antisymmetric stretching mode at 3670 cm^{-1}, useful to monitor the OH content [1]. The Si-OH concentration was evaluated by following the calibration procedures proposed for fused silica [42], based on the measurement of either the peak amplitude or the area subtended to the absorption band at 3670 cm^{-1}. The results are reported in Table 3. The high densification temperature of our synthesis leads to sol-gel glasses with very low content of OH groups if compared to similar samples treated at lower temperatures [43]. The drawing process turned out to positively induce a further reduction of the OH content, providing the desorption of most of the OH groups initially present and with a final hydroxil content comparable to sol-gel dehydrated bulk silica intentionally doped with fluorine [43, 44]. The presence of OH groups should indeed be limited because it can cause quenching of radiative recombinations [45].

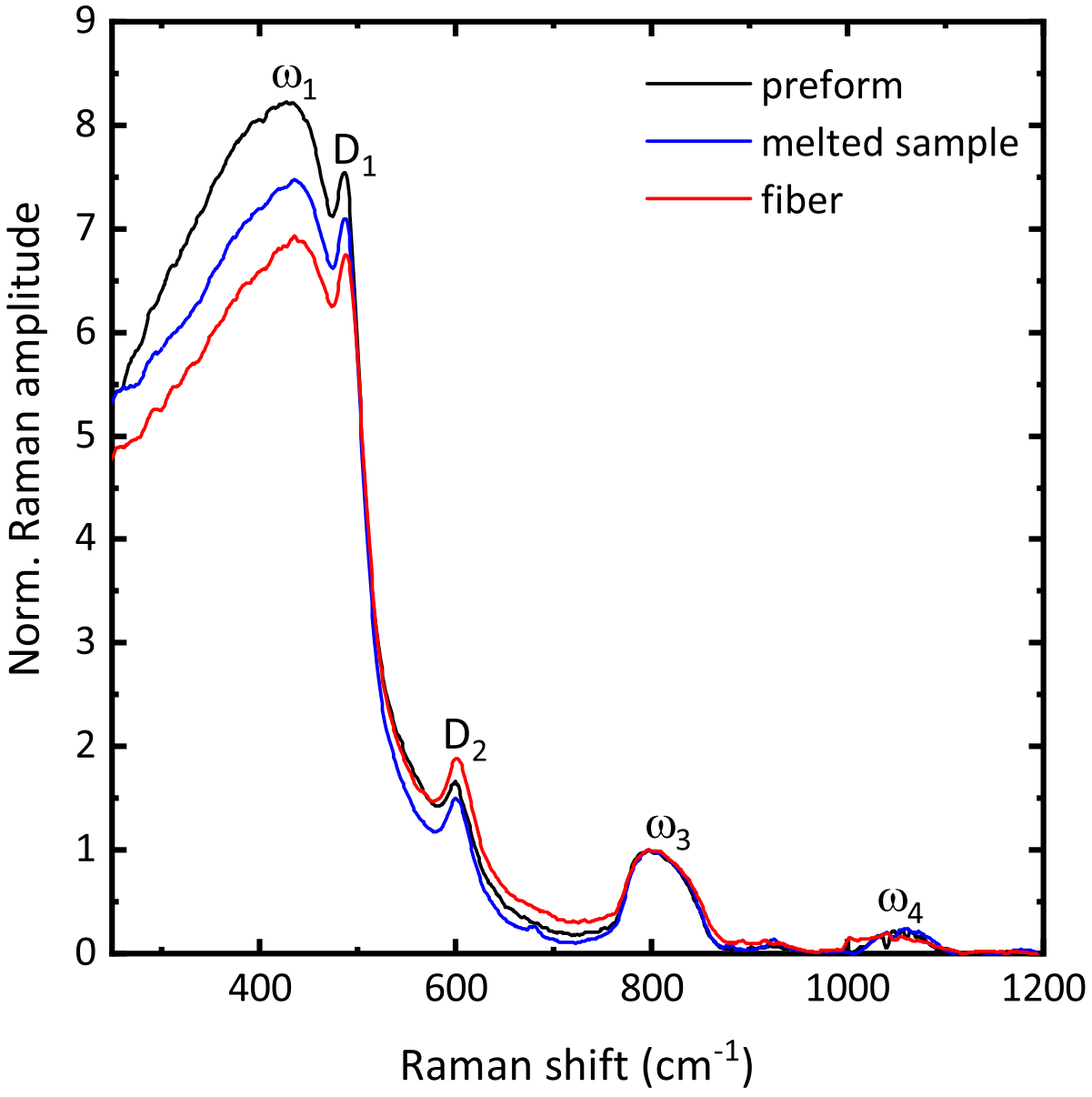

Figure 5: Raman spectra of sol-gel silica at various stages of the drawing process, as reported in the legend, normalized to the ω_3 band maximum.

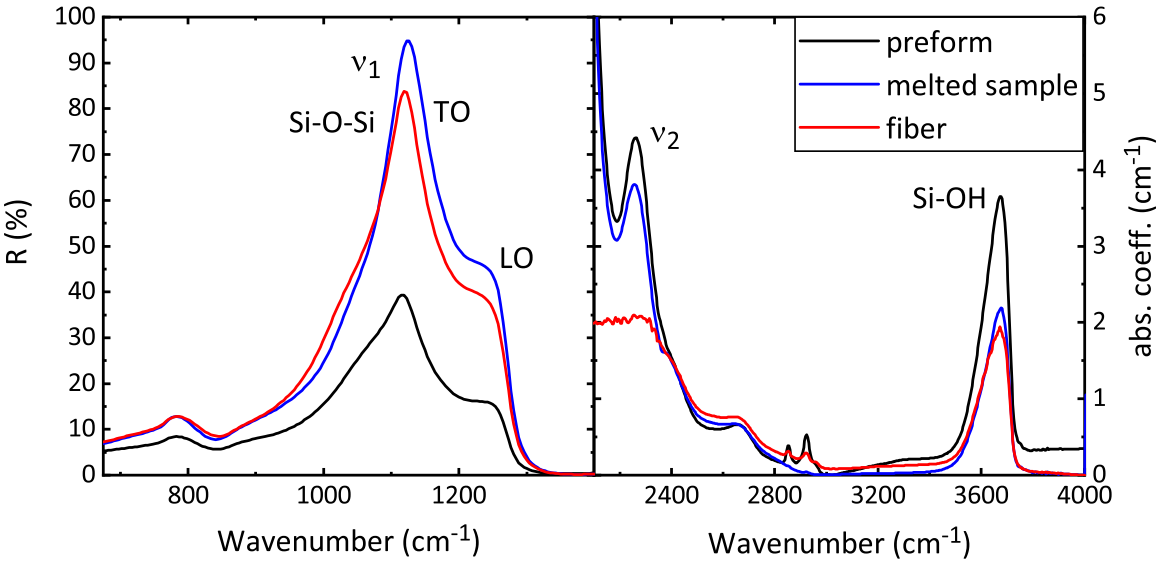

Figure 6: FTIR spectra obtained in reflection mode in the 400-2000 cm^{-1} range related to the fundamental band at 1120 cm^{-1} of the Si-O-Si bond antisymmetric stretching (left panel). FTIR spectra obtained in absorption mode in the 2000-4000 cm^{-1} range (right panel): the main features are related to the overtone of the fundamental band at 2260 cm^{-1} and to the Si-OH stretching mode at 3670 cm^{-1}. Silica samples coming from different stages of the drawing process, as listed in the legend, are compared.

3.3. Correlation between mechanical strengthening and vibrational properties

Raman spectroscopy may give useful information on the local microstructure and crystalline order of a material; moreover, it is a non-intrusive technique which, coupled to the nanoindentation method, provides a qualitative investigation of residual stresses in sol-gel silica. Indeed, peak shifting yields a direct relationship between process conditions and residual stresses. Tensile stresses stretch the lattice and cause the Raman active peaks to shift towards lower wavenumbers; on the other hand, compressive stresses cause peak shifting towards higher wavenumbers [46, 47], due to the enhanced compactness of the glass network. The wavenumber shift is in proportion to the magnitude of the residual stress. The observation of a slight shift of the D_1 and D_2 peaks to higher wavenumbers in Raman measurements, reported in detail in Table 2, thus supports the existence of compressive residual stresses in the fiber sample; moreover, it can be related to a tightening of the Si-O-Si bindings expected in well densified glasses [40, 48]. On the other hand, a definite trend in the peak shift of the fundamental Si-O-Si stretching mode and of its overtone cannot be clearly evidenced by FTIR measurements.

A strengthening of silica glass in the fiber shape is evidenced by the nanoindentation data: as already pointed out in the previous sections, an increase of the threshold load for cracks formation occurred in the fibers. An increase of the hardness of silica fibers with respect to the melted sample has also been demonstrated both by a shift in the load-displacement curves towards a lower maximum penetration depth with the same applied load, shown in Fig. 2(b), and by the increase of the parameters values reported in Table 1, resulting by the fit analysis of the unloading segments.

This evidence has been related to the existence of compressive stresses both by simulations [49] and experimental results [50]; moreover, residual stresses in the fiber cladding turned out to be less intense than in the fiber core, in relationship with the thermal and residual stress profiles arisen from the tension applied during fiber formation [51]. Therefore, we ascribe the observed silica hardening to the presence of compressive residual stresses in the fiber and to a densification of silica, both due to a rearrangement of the silica matrix occurring during fiber drawing [52] and leading to a more compact silica network. Indeed, a strengthening of silica fibers was obtained on purpose by Lezzi et al. [53], by heat-treating the fibers while holding them under a subcritical tensile stress, and was attributed to the formation of compressive stress layers created by a surface stress relaxation process.

Hence, we suggest that the fiber drawing process has induced the observed compressive residual stresses in the fibers, possibly caused either by the high temperature treatment under an applied tensile axial stress [54] or by the rapid cooling of the glass freezing the stresses in the material [10]; the thermal history experienced by the fibers could indeed have created axial, tangential, and radial stresses, which can be considered as a sum of thermoelastic and mechanical pulling [55]. Moreover, the differences in the coefficient of thermal expansion of the fluorinated silica cladding and the RE-doped fiber core could have contributed to the final fiber residual stresses [56]. To further reinforce the obtained results, future research could compare several drawing tests with different drawing speed, by choosing the same sample position along the fiber neck-down.

In addition, we can tentatively further relate the observed silica hardening to the decrease in the OH content reported in Table 3, as suggested in [57] for glassy films. The reduction of the OH concentration is a complementary effect of the drawing process, playing a role in the rearrangement of the silica matrix and leading to a strengthening of the material.

4. Conclusions

The mechanical properties of sol-gel silica glass have been investigated, considering different materials, from preforms to fibers through the intermediate samples taken from the fiber drawing neck-down. The use of the nanoindentation technique allowed to deepen the knowledge about the influence of the fiber drawing process, the X-ray irradiation, and the dopant specie on the mechanical properties of sol-gel silica glass; concerning the latter two factors, no clear dependence was evidenced. The comparison of the obtained results with a standard glass reference revealed that sol-gel silica shows good mechanical properties, consistent with those of the reference sample. Most notably, we also found that the fiber drawing positively influenced the silica hardness: the fiber form turned out to be harder and more resistant to the application of an external load, with respect to the preform it derived from, due to the existence of compressive residual stresses. On the other hand, also the complementary investigation of the vibrational properties of silica glass, carried out by Raman and FTIR spectroscopy, evidenced that the high temperature treatment combined with a quick cooling of the glass induced thermal stresses in the fibers, while also reducing their OH content.

Therefore, by coupling nanoindentation measurements and vibrational spectroscopy, a correlation can be established between the observed phenomena and the occurrence of a structural readjustment of the amorphous SiO_2 network, which occurs during the drawing process. The crucial role of the drawing-induced residual stresses on the structural properties of silica glass was thus demonstrated: the complementary experimental techniques employed in this work allowed to shed light on the correlation between structural, vibrational, and mechanical properties of sol-gel silica.

CRediT authorship contribution statement

Francesca Cova: conceptualization, writing – original draft, leading the main investigation, carrying out nanoindentation, Raman and FTIR measurements and their interpretation. **Alessandro Benedetto**: conceptualization, nanoindentation measurements and interpretation. **Norberto Chiodini**: samples synthesis. **Roberto Lorenzi**: Raman and FTIR measurements and interpretation. **Anna Vedda**: conceptualization, supervision, writing – review, discussion and interpretation of experimental data. Project administration. **Vladimir Ouspenski**: conceptualization, supervision, discussion and interpretation of experimental data. Project administration.

Declaration of Competing Interest

The authors declare that they have no conflict of interest or personal relationships that could have appeared to influence the work reported in this paper.

Acknowledgments

This work was supported primarily by the EIT SPARK project (Grant No. 16290) and by the EU-Project ATTRACT (Grant No. 777222).

References

[1] A. Vedda, N. Chiodini, D. Di Martino, M. Fasoli, F. Morazzoni, F. Moretti, R. Scotti, G. Spinolo, A. Baraldi, R. Capelletti, M. Mazzera, M. Nikl, Insights into microstructural features governing Ce^{3+} luminescence efficiency in sol-gel silica glasses, Chem. Mater. 18 (26) (2006) 6178–6185. doi:10.1021/cm0617541.

[2] D. Di Martino, A. Vedda, G. Angella, M. Catti, E. Cazzini, N. Chiodini, F. Morazzoni, R. Scotti, G. Spinolo, Evidences of rare earth ion aggregates in a sol-gel silica matrix: the case of Cerium and Gadolinium, Chem. Mater. 16 (17) (2004) 3352–3356. doi:10.1021/cm049276m.

[3] A. Vedda, N. Chiodini, M. Fasoli, A. Lauria, F. Moretti, D. Di Martino, A. Baraldi, E. Buffagni, R. Capelletti, M. Mazzera, P. Bohacek, E. Mihokova, Evidences of rare-earth nanophases embedded in silica using vibrational spectroscopy, IEEE Trans. Nucl. Sci. 57 (3) (2010) 1361–1369. doi:10.1109/tns.2010.2044420.

[4] F. Moretti, A. Vedda, N. Chiodini, M. Fasoli, A. Lauria, V. Jary, R. Kucerkova, E. Mihokova, A. Nale, M. Nikl, Incorporation of Ce^{3+} in crystalline Gd-silicate nanoclusters formed in silica, J. Lumin. 132 (2) (2012) 461–466. doi:10.1016/j.jlumin.2011.09.016.

[5] I. Veronese, C. De Mattia, M. Fasoli, N. Chiodini, E. Mones, M. C. Cantone, A. Vedda, Infrared luminescence for real time ionizing radiation detection, Appl. Phys. Lett. 105 (6) (2014) 061103. doi:10.1063/1.4892880.

[6] I. Veronese, N. Chiodini, S. Cialdi, E. d'Ippolito, M. Fasoli, S. Gallo, S. La Torre, E. Mones, A. Vedda, G. Loi, Real-time dosimetry with Yb-doped silica optical fibres, Phys. Med. Biol. 62 (10) (2017) 4218–4236. doi:10.1088/1361-6560/aa642f.

[7] F. Cova, F. Moretti, M. Fasoli, N. Chiodini, K. Pauwels, E. Auffray, M. T. Lucchini, S. Baccaro, A. Cemmi, H. Bártová, A. Vedda, Radiation hardness of Ce-doped sol-gel silica fibers for high energy physics applications, Opt. Lett. 43 (4) (2018) 903–906. doi:10.1364/ol.43.000903.

[8] F. Cova, M. T. Lucchini, K. Pauwels, E. Auffray, N. Chiodini, M. Fasoli, A. Vedda, Dual Cherenkov and scintillation response to high-energy electrons of rare-earth-doped silica fibers, Phys. Rev. Appl 11 (2) (2019) 024036. doi:10.1103/physrevapplied.11.024036.

[9] A. Mawardi, R. Pitchumani, Optical fiber drawing process model using an analytical neck-down profile, IEEE Photon. J. 2 (4) (2010) 620–629.

[10] U. C. Paek, C. R. Kurkjian, Calculation of cooling rate and induced stresses in drawing of optical fibers, J. Am. Ceram. Soc. 58 (7-8) (1975) 330–335. doi:10.1111/j.1151-2916.1975.tb11490.x.

[11] R. Gardon, Glass Science and Technology, Elsevier, 1980, Ch. Thermal Tempering of Glass, pp. 145–216. doi:10.1016/b978-0-12-706705-6.50010-2.

[12] Y. Hibino, F. Hanawa, M. Horiguchi, Drawing-induced residual stress effects on optical characteristics in pure-silica-core single-mode fibers, J. Appl. Phys. 65 (1) (1989) 30–34. doi:10.1063/1.342542.

[13] A. D. Yablon, Optical Fiber Communication Conference, Vol. 1, Optical Society of America, Washington, D.C, 2004, Ch. Stresses and strains frozen into optical fibers, pp. 325–327.

[14] A. Vedda, N. Chiodini, D. Di Martino, M. Fasoli, S. Keffer, A. Lauria, M. Martini, F. Moretti, G. Spinolo, M. Nikl, N. Solovieva, G. Brambilla, Ce^{3+}-doped fibers for remote radiation dosimetry, Appl. Phys. Lett. 85 (26) (2004) 6356–6358. doi:10.1063/1.1840127.

[15] B. Brichard, P. Borgermans, A. Fernandez, K. Lammens, A. Decreton, Radiation effect in silica optical fiber exposed to intense mixed neutron-gamma radiation field, IEEE Transactions on Nuclear Science 48 (6) (2001) 2069–2073. doi:10.1109/23.983174.

[16] A. Alessi, S. Girard, M. Cannas, S. Agnello, A. Boukenter, Y. Ouerdane, Influence of drawing conditions on the properties and radiation sensitivities of pure-silica-core optical fibers, Journal of Lightwave Technology 30 (11) (2012) 1726–1732. doi:10.1109/jlt.2012.2188827.

[17] S. Girard, J. Kuhnhenn, A. Gusarov, B. Brichard, M. V. Uffelen, Y. Ouerdane, A. Boukenter, C. Marcandella, Radiation effects on silica-based optical fibers: Recent advances and future challenges, IEEE Transactions on Nuclear Science 60 (3) (2013) 2015–2036. doi:10.1109/tns.2012.2235464.

[18] E. J. Friebele, R. E. Jaeger, G. H. Sigel, M. E. Gingerich, Effect of ionizing radiation on the optical attenuation in polymer-clad silica fiber-optic waveguides, Appl. Phys. Lett. 32 (2) (1978) 95–97. doi:10.1063/1.89949.

[19] F. Cova, M. Fasoli, F. Moretti, N. Chiodini, K. Pauwels, E. Auffray, M. T. Lucchini, E. Bourret, I. Veronese, E. d'Ippolito, A. Vedda, Optical properties and radiation hardness of Pr-doped sol-gel silica: Influence of fiber drawing process, J. Lumin. 192 (2017) 661–667. doi:10.1016/j.jlumin.2017.07.045.

[20] M. Vukcevich, A new interpretation of the anomalous properties of vitreous silica, J. Non-Cryst. Solids 11 (1) (1972) 25–63. doi:10.1016/0022-3093(72)90305-5.

[21] Z. Burghard, A. Zimmermann, J. Rödel, F. Aldinger, B. R. Lawn, Crack opening profiles of indentation cracks in normal and anomalous glasses, Acta Mater. 52 (2) (2004) 293–297. doi:10.1016/j.actamat.2003.09.014.

[22] A. Arora, D. Marshall, B. Lawn, M. Swain, Indentation deformation/fracture of normal and anomalous glasses, J. Non-Cryst. Solids 31 (3) (1979) 415–428. doi:10.1016/0022-3093(79)90154-6.

[23] W. Oliver, G. Pharr, Measurement of hardness and elastic modulus by instrumented indentation: Advances in understanding and refinements to methodology, J. Mater. Res. 19 (1) (2004) 3–20. doi:10.1557/jmr.2004.19.1.3.

[24] C. A. Schneider, W. S. Rasband, K. W. Eliceiri, NIH image to ImageJ: 25 years of image analysis, Nat. Methods 9 (7) (2012) 671–675. doi:10.1038/nmeth.2089.

[25] A. Fischer-Cripps, Critical review of analysis and interpretation of nanoindentation test data, Surf. Coat. Technol. 200 (14-15) (2006) 4153–

4165. doi:10.1016/j.surfcoat.2005.03.018.

[26] A. Koike, S. Akiba, T. Sakagami, K. Hayashi, S. Ito, Difference of cracking behavior due to vickers indentation between physically and chemically tempered glasses, J. Non-Cryst. Solids 358 (24) (2012) 3438–3444. doi:10.1016/j.jnoncrysol.2012.02.020.

[27] R. Tandon, A technique for measuring stresses in small spatial regions using cube-corner indentation: Application to tempered glass plates, J. Eur. Ceram. Soc. 27 (6) (2007) 2407–2414. doi:10.1016/j.jeurceramsoc.2006.09.001.

[28] G. Anstis, P. Chantikul, B. Lawn, D. Marshall, A critical evaluation of indentation techniques for measuring fracture toughness: I, direct crack measurements, J. Am. Ceram. Soc. 64 (9) (1981) 533–538. doi:10.1111/j.1151-2916.1981.tb10320.x.

[29] K. Gadelrab, F. Bonilla, M. Chiesa, Densification modeling of fused silica under nanoindentation, J. Non-Cryst. Solids 358 (2) (2012) 392–398. doi:10.1016/j.jnoncrysol.2011.10.011.

[30] W. Oliver, G. Pharr, An improved technique for determining hardness and elastic modulus using load and displacement sensing indentation experiments, J. Mater. Res. 7 (6) (1992) 1564–1583. doi:10.1557/jmr.1992.1564.

[31] J. H. Westbrook, Phys. Chem. Glasses 1 (1960) 32.

[32] A. E. Geissberger, F. L. Galeener, Raman studies of vitreous SiO_2 versus fictive temperature, Phys. Rev. B 28 (6) (1983) 3266–3271. doi:10.1103/physrevb.28.3266.

[33] F. Galeener, Planar rings in glasses, Solid State Commun. 44 (7) (1982) 1037–1040. doi:10.1016/0038-1098(82)90329-5.

[34] F. L. Galeener, Band limits and the vibrational spectra of tetrahedral glasses, Phys. Rev. B 19 (8) (1979) 4292–4297. doi:10.1103/physrevb.19.4292.

[35] C. A. Murray, T. J. Greytak, Intrinsic surface phonons in amorphous silica, Phys. Rev. B 20 (8) (1979) 3368–3387. doi:10.1103/physrevb.20.3368.

[36] A. Vedda, A. Baraldi, C. Canevali, R. Capelletti, N. Chiodini, R. Francini, M. Martini, F. Morazzoni, M. Nikl, R. Scotti, G. Spinolo, Optical properties of Ce^{3+}-doped sol–gel silicate glasses, Nucl. Instrum. Methods Phys. Res., Sect. A 486 (1-2) (2002) 259–263. doi:10.1016/s0168-9002(02)00713-1.

[37] A. Pasquarello, R. Car, Identification of Raman defect lines as signatures of ring structures in vitreous silica, Phys. Rev. Lett. 80 (23) (1998) 5145–5147. doi:10.1103/physrevlett.80.5145.

[38] J. Mikkelsen, F. Galeener, Thermal equilibration of raman active defects in vitreous silica, J. Non-Cryst. Solids 37 (1) (1980) 71–84. doi:10.1016/0022-3093(80)90480-9.

[39] T. Deschamps, A. Kassir-Bodon, C. Sonneville, J. Margueritat, C. Martinet, D. de Ligny, A. Mermet, B. Champagnon, Permanent densification of compressed silica glass: a raman-density calibration curve, J. Phys.: Condens. Matter 25 (2) (2012) 025402. doi:10.1088/0953-8984/25/2/025402.

[40] J. Burgin, C. Guillon, P. Langot, F. Vallée, B. Hehlen, M. Foret, Vibrational modes and local order in permanently densified silica glasses: Femtosecond and raman spectroscopy study, Phys. Rev. B 78 (18) (2008) 184203. doi:10.1103/physrevb.78.184203.

[41] G. E. Walrafen, P. N. Krishnan, S. W. Freiman, Raman investigation of optical fibers under high tensile stress, J. Appl. Phys. 52 (4) (1981) 2832–2836. doi:10.1063/1.329013.

[42] K. Davis, A. Agarwal, M. Tomozawa, K. Hirao, Quantitative infrared spectroscopic measurement of hydroxyl concentrations in silica glass, J. Non-Cryst. Solids 203 (1996) 27–36. doi:10.1016/0022-3093(96)00330-4.

[43] N. Chiodini, A. Lauria, R. Lorenzi, S. Brovelli, F. Meinardi, A. Paleari, Sol–gel strategy for self-induced fluorination and dehydration of silica with extended vacuum ultraviolet transmittance and radiation hardness, Chem. Mater. 24 (4) (2012) 677–681. doi:10.1021/cm202664a.

[44] A. Paleari, F. Meinardi, A. Lauria, R. Lorenzi, N. Chiodini, S. Brovelli, High-energy shift of the urbach ultraviolet absorption from attenuated dynamical disorder in fluorine modified sol-gel silica, Appl. Phys. Lett. 91 (14) (2007) 141913. doi:10.1063/1.2794429.

[45] A. Baraldi, R. Capelletti, N. Chiodini, C. Mora, R. Scotti, E. Uccellini, A. Vedda, Vibrational spectroscopy of OH-related groups in Ce^{3+}- and Gd^{3+}-doped silicate glasses, Nucl. Instrum. Methods Phys. Res., Sect. A 486 (1-2) (2002) 408–411. doi:10.1016/s0168-9002(02)00743-x.

[46] C. A. Taylor, M. F. Wayne, W. K. Chiu, Residual stress measurement in thin carbon films by Raman spectroscopy and nanoindentation, Thin

Solid Films 429 (1-2) (2003) 190–200. doi:10.1016/s0040-6090(03)00276-1.

[47] A. Perriot, D. Vandembroucq, E. Barthel, V. Martinez, L. Grosvalet, C. Martinet, B. Champagnon, Raman microspectroscopic characterization of amorphous silica plastic behavior, J. Am. Ceram. Soc. 89 (2) (2006) 596–601. doi:10.1111/j.1551-2916.2005.00747.x.

[48] D. Vandembroucq, T. Deschamps, C. Coussa, A. Perriot, E. Barthel, B. Champagnon, C. Martinet, Density hardening plasticity and mechanical ageing of silica glass under pressure: a raman spectroscopic study, J. Phys.: Condens. Matter 20 (48) (2008) 485221. doi:10.1088/0953-8984/20/48/485221.

[49] T. Buchheit, R. Tandon, Measuring residual stress in glasses and ceramics using instrumented indentation, J. Mater. Res. 22 (10) (2007) 2875–2887. doi:10.1557/jmr.2007.0358.

[50] J. G. Swadener, B. Taljat, G. Pharr, Measurement of residual stress by load and depth sensing indentation with spherical indenters, J. Mater. Res. 16 (7) (2001) 2091–2102. doi:10.1557/jmr.2001.0286.

[51] D. J. Wissuchek, C. W. Ponader, J. J. Price, Analysis of residual stress in optical fiber, in: M. J. Matthewson (Ed.), Optical Fiber Reliability and Testing, SPIE, 1999, pp. 34–43. doi:10.1117/12.372783.

[52] A. Alessi, S. Girard, C. Marcandella, M. Cannas, A. Boukenter, Y. Ouerdane, Raman investigation of the drawing effects on ge-doped fibers, J. Non-Cryst. Solids 357 (1) (2011) 24–27. doi:10.1016/j.jnoncrysol.2010.09.080.

[53] P. Lezzi, Q. Xiao, M. Tomozawa, T. Blanchet, C. Kurkjian, Strength increase of silica glass fibers by surface stress relaxation: A new mechanical strengthening method, J. Non-Cryst. Solids 379 (2013) 95–106. doi:10.1016/j.jnoncrysol.2013.07.033.

[54] P. Lezzi, M. Tomozawa, R. Hepburn, Confirmation of thin surface residual compressive stress in silica glass fiber by FTIR reflection spectroscopy, J. Non-Cryst. Solids 390 (2014) 13–18. doi:10.1016/j.jnoncrysol.2014.02.021.

[55] P. Y. Fonjallaz, F. Cochet, B. Leuenberger, H. G. Limberger, R. P. Salathé, Tension increase correlated to refractive-index change in fibers containing UV-written bragg gratings, Opt. Lett. 20 (11) (1995) 1346–1348. doi:10.1364/ol.20.001346.

[56] C. R. Kurkjian, U. C. Paek, Effect of drawing tension on residual stresses in clad glass fibers, J. Am. Ceram. Soc. 61 (3-4) (1978) 176–177. doi:10.1111/j.1151-2916.1978.tb09267.x.

[57] I. Yakimets, N. Wellner, A. C. Smith, R. H. Wilson, I. Farhat, J. Mitchell, Mechanical properties with respect to water content of gelatin films in glassy state, Polymer 46 (26) (2005) 12577–12585. doi:10.1016/j.polymer.2005.10.090.

Graphical abstract